Photon shell game in three-resonator circuit quantum electrodynamics

Matteo Mariantoni[1,3,*], H. Wang[1], Radoslaw C. Bialczak[1], M. Lenander[1], Erik Lucero[1], M. Neeley[1], A. D. O'Connell[1], D. Sank[1], M. Weides[1], J. Wenner[1], T. Yamamoto[1,2], Y. Yin[1], J. Zhao[1], John M. Martinis[1,†] and A. N. Cleland[1,‡]

[1]**Department of Physics, University of California, Santa Barbara, California 93106, USA**

[2]**Green Innovation Research Laboratories, NEC Corporation, Tsukuba, Ibaraki 305-8501, Japan**

[3]**California NanoSystems Institute, University of California, Santa Barbara, California 93106, USA**

[*]**e-mail: matmar@physics.ucsb.edu**

[†]**e-mail: martinis@physics.ucsb.edu**

[‡]**e-mail: anc@physics.ucsb.edu**

last updated: February 15, 2022

The generation and control of quantum states of light constitute fundamental tasks in cavity quantum electrodynamics (QED)[1–10]. The superconducting realization of cavity QED, circuit QED[11–14], enables on-chip microwave photonics, where superconducting qubits[15–18] control and measure individual photon states[19–26]. A long-standing issue in cavity QED is the coherent transfer of photons between two or more resonators. Here, we use circuit QED to implement a three-resonator architecture on a single chip, where the resonators are interconnected by two superconducting phase qubits. We use this circuit to shuffle one- and two-photon Fock states between the three resonators, and demonstrate qubit-mediated vacuum Rabi swaps between two resonators. This illustrates the potential for using multi-resonator circuits as photon quantum registries and for creating multipartite entanglement between delocalized bosonic modes[27].

The combination of high-finesse electromagnetic cavities with atoms or qubits enables fundamental studies of the interaction between light and matter. The cavity provides a protected environment for storing and tailoring individual photonic excitations[1–3,14]. Both stationary[6,23] and propagating[7,9] nonclassical fields can be synthesized using such systems, enabling quantum memory and quantum messaging[8]. A critical challenge however is the extension from single to more versatile multi-cavity architectures[27,29], allowing manipulation of spatially separated bosonic modes. While the entanglement of different modes of a single cavity has been shown in atomic systems[4,10], and a coupled low- and high-quality factor resonator studied in circuit QED[25,26], coherent dynamics between two or more high-quality factor cavities has yet to be demonstrated. Here we describe a triple-resonator system, where three high-quality factor microwave resonators are coupled to two superconducting phase qubits (cf. Fig. 1). The qubits serve as quantum transducers that create and transfer photonic states between the resonators[28]. The quantum transduction is performed by means of purely *resonant* qubit-resonator interactions, rather than dispersive coupling[27], enabling rapid transfers between resonators with significantly different frequencies. As an important example, we demonstrate single-photon Rabi swaps between two resonators de-tuned by $\simeq 12000$ resonator linewidths.

Figure 1a,b shows the main experimental elements, which comprise three coplanar waveguide resonators, R_a, R_b and R_c, two phase qubits, Q_1 and Q_2, and two superconducting quantum interference devices (SQUIDs) used for qubit state readout. Each qubit is coupled to a control line which is used to
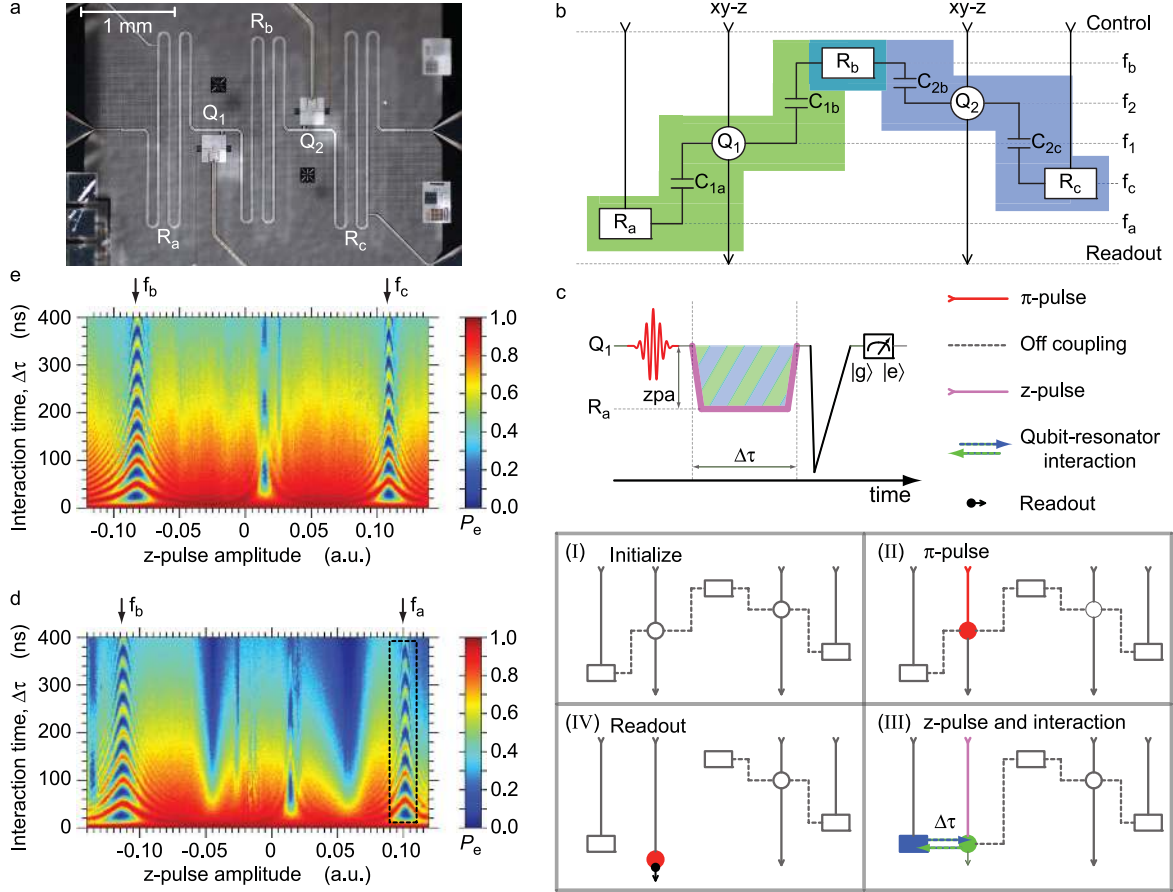
Figure 1: **Experimental architecture and two-dimensional swap spectroscopy. a,** Optical micrograph of sample, showing three coplanar waveguide resonators (R_a, R_b and R_c, with meander design) capacitively coupled to two super-conducting phase qubits (Q_1 and Q_2, in boxes). **b,** Block diagram showing main elements, which comprise two circuit unit cells R_a-Q_1-R_b (light green area) and R_b-Q_2-R_c (dark blue area). The horizontal placement represents the spatial layout of the sample, whereas the vertical distribution corresponds to the frequencies of the elements. The qubit-resonator coupling capacitors are designed to be $C_{1a} = C_{1b} = C_{2b} = C_{2c} = 1.9\,fF$. $f_a \simeq 6.29\,GHz$, $f_b \simeq 6.82\,GHz$ and $f_c \simeq 6.34\,GHz$ are the measured resonator frequencies, and f_1 and f_2 the tuneable qubit transition frequencies. Control and readout wiring is also shown. **c,** Upper sub-panel, pulse sequence for swap spectroscopy, with data shown in **d** and **e**. Q_1 line shows Gaussian microwave π-pulse (red) and qubit tuning pulse (z-pulse; hashed magenta) with variable z-pulse amplitude zpa and duration $\Delta\tau$, followed by a triangular measurement pulse (black). Lower sub-panel, diagrammatic representation of the pulse sequence. (I) The entire system is initialized in the ground state. (II) Q_1 is excited by a π-pulse (red), then (III) brought into resonance with R_a via a z-pulse (magenta) and allowed to interact with the resonator for a time $\Delta\tau$. (IV) A measurement pulse projects the qubit onto its ground state $|g\rangle$ or excited state $|e\rangle$. **d,** Two-dimensional swap spectroscopy for Q_1. The probability P_e to find the qubit in $|e\rangle$ is plotted versus z-pulse amplitude and resonator measurement time $\Delta\tau$. The typical chevron pattern generated by a qubit-resonator swap (arrows) is evident for both the Q_1-R_a (dashed black box) and Q_1-R_b interactions. Near the center of the plot a qubit interaction with a spurious two-level system is seen, surrounded by two regions with short qubit relaxation time. **e,** Same as **d** for Q_2. From these measurements, we find the coupling strengths $g_{1a} \simeq 17.58 \mp 0.01\,MHz$, $g_{1b} \simeq 20.65 \mp 0.02\,MHz$, $g_{2b} \simeq 20.43 \mp 0.01\,MHz$ and $g_{2c} \simeq 17.96 \mp 0.01\,MHz$.

adjust the qubit operating frequency $f_{1,2}$ and couple microwave pulses for controlling and measuring the qubit state. During operation, the device is attached to the mixing chamber of a dilution refrigerator at $\approx 25\,mK$.

The circuit layout (Fig. 1b) can be decomposed into two unit cells, R_a-Q_1-R_b (green area) and R_b-Q_2-R_c (blue area). The shared resonator R_b connects the two cells and protects the two qubits from unwanted crosstalk. The resonator frequencies f_a, f_b and f_c are measured with qubit spectroscopy (not shown). The vacuum Rabi couplings between each qubit and its corresponding resonators, g_{1a} and g_{1b} for Q_1 and g_{2b} and g_{2c} for Q_2, are determined by their respective coupling capacitors (cf. Fig. 1b). The coupling strengths are measured using two-dimensional swap spectroscopy (cf. Fig.1d,e). We note that the swap spectroscopy provides an excellent tool for revealing the presence of spurious two-level systems
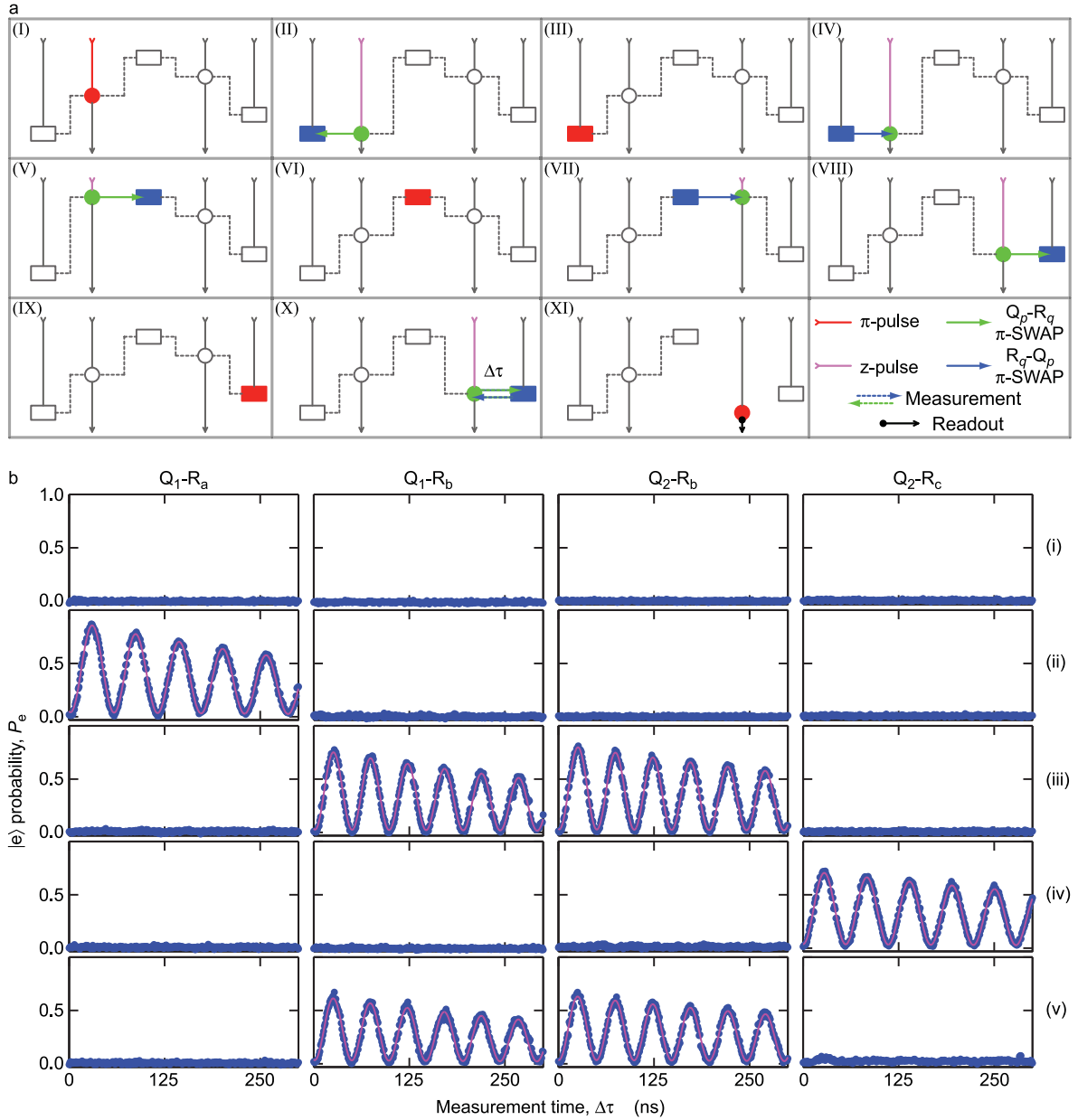
Figure 2: **Photon shell game. a,** Block diagram of the sequence used to coherently transfer a single photon Fock state $|1\rangle$ from R_a to R_c via R_b. After initializing the system in the ground state, (I), Q_1 is excited by a π-pulse and, (II), z-pulsed into resonance with R_a for a full Rabi swap (Rabi π-swap) at the end of which, (III), R_a is populated by the one-photon Fock state $|1\rangle$ and Q_1 is in its ground state, at the idle point. In (IV), Q_1 is z-pulsed into resonance with R_a for a Rabi π-swap and then, (V), z-pulsed into resonance with R_b for another Rabi π-swap at the end of which, (VI), R_b is populated by the one-photon Fock state and both Q_1 and Q_2 are in the ground state at the idle point. (VII), Q_2 is z-pulsed into resonance with R_b for a Rabi π-swap and, (VIII), z-pulsed into resonance with R_c for another Rabi π-swap at the end of which, (IX), R_c is in the one-photon Fock state and Q_2 in the ground state at the idle point. Measurement and qubit state readout are performed in (X) and (XI), respectively, where the presence of the Fock state in R_c is detected by its interaction with Q_2. **b,** Measurement outcomes for different photon shell games. Each plot shows the probability P_e to measure a qubit in the excited state $|e\rangle$ as a function of the qubit-resonator measurement time $\Delta\tau$. Blue circles are data, magenta lines a least-squares fit. Data for Q_1 are in the first two columns, for Q_2 in the second two; each row corresponds to a different game. Row (i), all resonators are in the vacuum state (with fidelity $\mathcal{F} > 0.99$; we define $\mathcal{F}$ as the amplitude of the fit; see Supplementary Information), i.e. no stored photons. Row (ii), resonator R_a contains one photon ($\mathcal{F} = 0.86 \mp 0.01$), with the other two resonators in the vacuum state. In row (iii) the photon has been placed in R_b ($\mathcal{F} = 0.80 \mp 0.01$), and in (iv) the photon is in resonator R_c ($\mathcal{F} = 0.69 \mp 0.01$). In (v), we have taken the photon from R_c and placed it back in R_b ($\mathcal{F} = 0.61 \mp 0.01$), demonstrating the high degree of control and coherence in the system.

(TLSs) as well as frequencies with short qubit relaxation times. In all the experiments, the qubits are initialized in the ground state $|g\rangle$ and are typically tuned to the idle point, where the qubit Q_1 (Q_2)
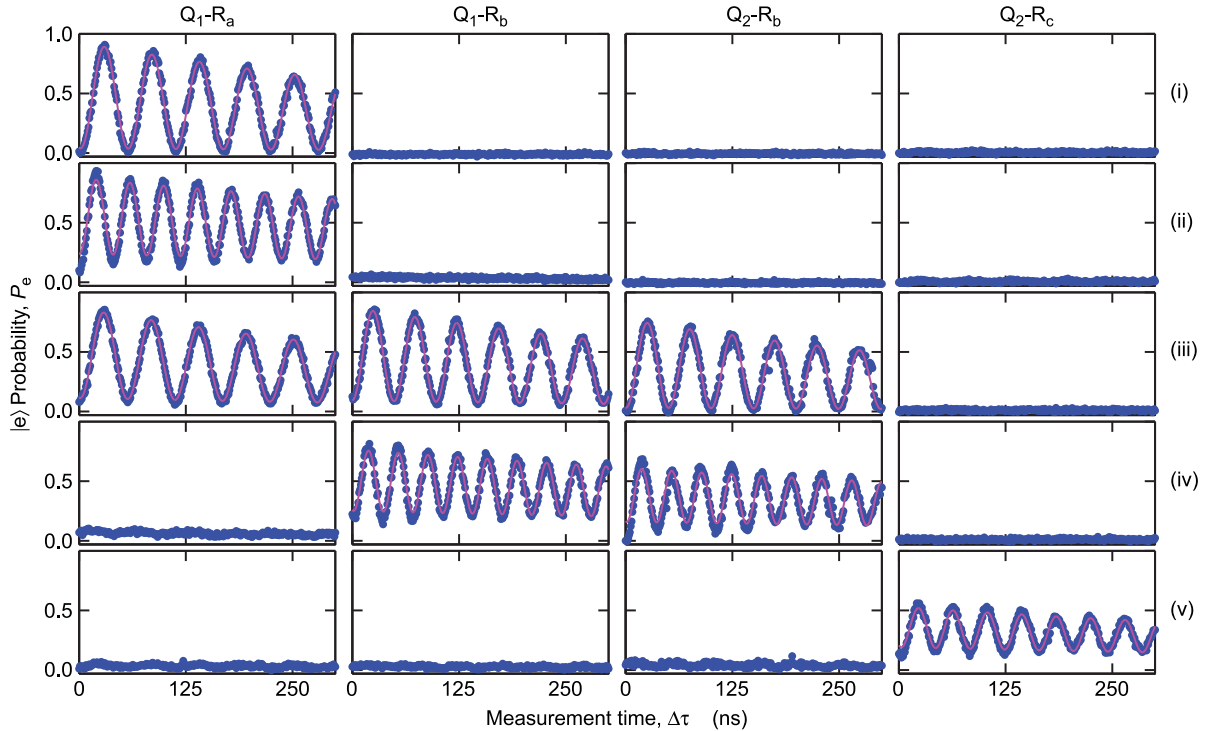
Figure 3: **Quantum-mechanical realization of the 'Towers of Hanoi'.** Format as in Fig. 2b, showing the probability P_e of measuring Q_1 or Q_2 in the excited state as a function of interaction time $\Delta\tau$ with a resonator. Data are shown as blue circles, with a least-squares fit as magenta solid lines. (i), A one-photon Fock state $|1\rangle$ in R_a with both R_b and R_c in the vacuum state, and (ii) a two-photon Fock state in R_a (fidelity $\mathcal{F} = 0.63 \mp 0.01$) with the other two resonators in the vacuum state. A qubit-resonator interaction oscillation is $\sqrt{2}$ faster for a two-photon state compared to a one-photon state. In (iii), one photon has been transferred from R_a to R_b, so one-photon oscillations are seen when Q_1 measures R_a or R_b, and when Q_2 measures R_b. In (iv), the second photon has been transferred to R_b ($\mathcal{F} = 0.51 \mp 0.01$), yielding the $\sqrt{2}$ increase when either Q_1 or Q_2 measure R_b. In (v), both photons have been transferred to R_c ($\mathcal{F} = 0.34 \mp 0.01$). Note that even with this complex protocol, both R_a and R_b display negligible oscillations ($\mathcal{F} \gtrsim 0.97$). See Supplementary Information for further analysis.

$|g\rangle \leftrightarrow |e\rangle$ transition frequency f_1 (f_2) is set in-between, and well away from, the resonator transition frequencies f_a and f_b (f_b and f_c).

When Q_1 (Q_2) is at the idle point, the qubit-resonator detuning is sufficiently large that the qubit-resonator interactions are effectively switched off. A particular qubit-resonator Q_p-R_q ($p = 1, 2$ and $q = a, b, c$) interaction is switched on by shifting the qubit transition frequency f_p to equal the resonator frequency f_q, setting the de-tuning to zero and enabling quantum energy transfers. The time-dependent control of the qubit transition frequency thus enables highly complex quantum control of the resonators [23].

Figure 2a shows a diagram of the pulse sequence used to implement the single photon equivalent of the 'shell game', in which a pea is hidden under one of three shells and the contestant must guess where the pea is after the shells have been shuffled. The three resonators play the role of the shells and a single photon Fock state $|1\rangle$ that of the pea. The system is initialized in the ground state, with the qubits at their idle points, so that all interactions are effectively switched off. Qubit Q_1 is used to pump a single photon into resonator R_a [Figure 2a(I-III)]. The photon state can then be transferred to either of the other two resonators, using the qubits in a similar fashion to mediate the single-excitation transfer. A transfer from R_a to R_b is shown in steps (IV-VI), and a second transfer from R_b to R_c performed using Q_2 in steps (VII-IX). The final location of the photon can be determined by employing the qubits as photon detectors, through the Rabi oscillations that occur when a qubit is brought in resonance with a resonator storing a photons [steps (X-XI)].

In the data shown in Figure 2b(i)-(v), which represents different versions of the game, a photon was
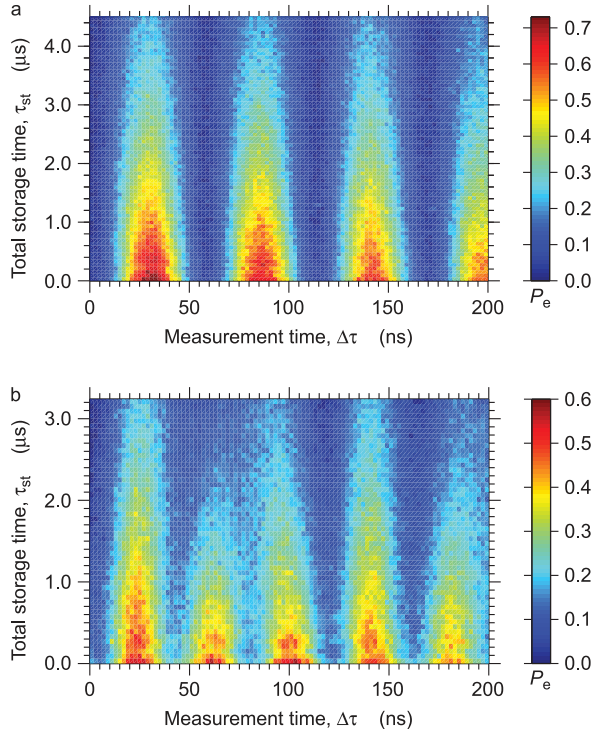
Figure 4: **Combined quantum state transfer and storage for one- and two-photon states. a,** Probability P_e to find Q_2 in the excited state (colour bar scale, right side) versus measurement time $\Delta\tau$ (horizontal axis), and total storage time τ_{st} (vertical axis). A one-photon Fock state is created and stored in resonator R_a for a time $\tau_{st}/3$, transferred to R_b and stored for the same time, then transferred to R_c, stored for the same time and then measured. **b,** Same as in **a,** but for the generation and storage of a two-photon Fock state.

stored in one of the three resonators, shuffled between the resonators, and all three resonators then measured. In the shell game of Fig. 2b(i), no photon was placed in any resonator, while for example in game (iv), a single photon was transferred from R_a to R_c via R_b, and then detected using qubit Q_2; measurements of the other resonators R_a and R_b show no oscillations, i.e. no photonic excitation.

We also explored a variant of the shell game, transferring a two-photon Fock state $|2\rangle$ from R_a to R_b to R_c. The two-photon Fock state is first generated in R_a[21], as shown by the measurements in Fig. 3(i),(ii). Figure 3 also shows the measurements after this state is transferred from R_a to R_b and then to R_c. Each transfer takes two steps, starting with e.g. the state $|Q_1 R_a R_b\rangle = |g20\rangle$. The qubit is brought into resonance with R_a, and one photon is Rabi-swapped to the qubit, at a rate $\sqrt{2}$ faster than the usual one-photon rate[21], leaving the system in the state $|e10\rangle$. The qubit is then tuned into resonance with resonator R_b for a one-photon Rabi swap, resulting in the state $|g11\rangle$ [Fig. 3(iii)]. The qubit is subsequently placed back in resonance with R_a for a one-photon swap, yielding $|e01\rangle$, and brought into resonance with R_b to transfer the second photon, ending with the state $|g02\rangle$ [Fig. 3(iv)]. To finally transfer the photons to resonator R_c, the process is repeated using qubit Q_2, which completes the full transfer of Fock state $|2\rangle$ [Fig. 3(v)]. This process resembles the well-known game 'The towers of Hanoi', where a set of disks with different diameters has to be moved between three posts (the three resonators) while maintaining the larger disks (Fock state $|1\rangle$, with the longer swapping time) always at the bottom of each post, and the smaller disks (Fock state $|2\rangle$, with shorter swapping time) on top.

A fundamental question for resonator-based quantum computing is whether quantum states can be stored in a resonator and later extracted and/or stored elsewhere. We demonstrate this functionality in Fig. 4, where a single photon is stored in each of the three resonators for a variable time $\tau_{st}/3$ before being transferred to the next resonator. Qubit measurements of the resonator containing the photon display clear oscillations for total storage times longer than $3\,\mu$s. Figure 4b is the same experiment
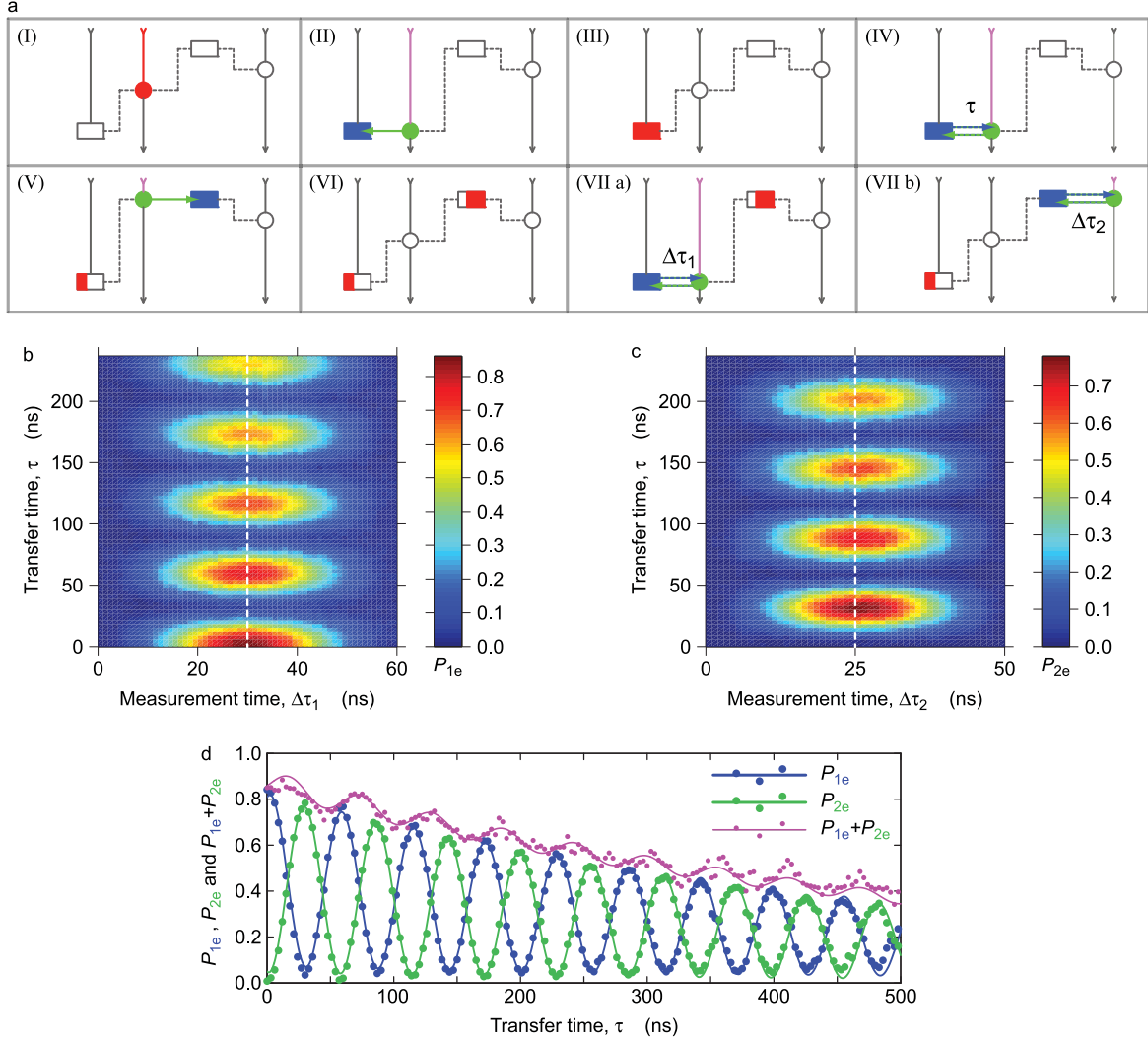
5

Figure 5: **Two-resonator Rabi swaps. a,** Block diagram of the preparation and measurement protocol. (I), Q_1 is excited by a π-pulse and, (II), brought into resonance with R_a for a Rabi π-swap, at the end of which, (III), R_a is populated by a one-photon Fock state. In (IV), Q_1 is brought into resonance with R_a for a variable transfer time τ at the end of which, (V), R_a is left partially populated, while, (V) and (VI), the remaining energy is fully transferred to R_b via a Rabi π-swap with Q_1. The probabilities for having the photon in R_a or R_b can be varied continuously by changing the transfer time τ (cf. main text). These probabilities are simultaneously measured for R_a with Q_1 (VII a) and for R_b with Q_2 (VII b). **b,** Qubit probability P_{1e} (colour scale bar) as a function of the Q_1-R_a measurement time $\Delta\tau_1$ (horizontal axis) and the transfer time τ (vertical axis). **c,** Same as **b**, but for Q_2's probability P_{2e} as a function of the Q_2-R_b measurement time $\Delta\tau_2$. Measurement times are sufficient to display one complete Rabi oscillation between the measurement qubit and resonator, with a Rabi swap occurring at the center of each horizontal axis (dashed white line), with multiple swaps displayed as a function of the Q_1-R_a transfer time τ (vertical direction). Cuts through the probabilities along the dashed white lines (full Rabi swaps) are shown in **d**, where the expected co-sinusoidal oscillations are observed in Q_1's probability P_{1e} (dark blue circles) (Q_2's probability P_{2e}, light green circles), with the summed probability $P = P_{1e} + P_{2e}$ (magenta circles) showing the expected slow decay (cf. main text). Solid lines are fits to data.

repeated with a two-photon Fock state. Clear oscillations are visible for total storage times longer than $1.5\,\mu$s. These experiments demonstrate the realization of a programmable quantum information register.

We further show that we can generate quantum state entanglement between the two resonators R_a and R_b. The protocol is diagrammed in Fig. 5a. A one-photon Fock state is first stored in R_a, placing the system in the state $|Q_1 R_a R_b\rangle = |g10\rangle$ [Fig. 5a(I)-(III)]. The qubit is then used to perform a partial transfer of the photon to R_b, achieved by placing Q_1 in resonance with R_a and varying the transfer time τ [Fig. 5a(IV)]. This leaves the system in the entangled state $\alpha|g10\rangle + \beta|e00\rangle$, with amplitudes[30] $\alpha = \cos(\pi g_{1a}\tau)$ and $\beta = i\sin(\pi g_{1a}\tau)$. The qubit frequency f_1 is then tuned from f_a to f_b, and left there

for a time equal to the Q_1-R_b swap time, thus mapping the qubit state onto the resonator and resulting in the two-resonator entangled state

$$\alpha|g10\rangle + \beta|g01\rangle = |g\rangle \otimes (\alpha|10\rangle + \beta|01\rangle).$$

We then use both qubits to simultaneously measure the two resonators, Q_1 measuring R_a for a measurement time $\Delta\tau_1$ and Q_2 measuring R_b for a time $\Delta\tau_2$. Figure 5b(c) shows the resulting oscillations in P_{1e} (P_{2e}) for Q_1 (Q_2) (colour bar scale), as a function of the measurement time (horizontal axis) and Q_1-R_a transfer time τ (vertical axis). The data display a single Rabi oscillation along the horizontal axis, which would repeat if the measurement time were increased, and also shows clear swaps as a function of the transfer time τ, as expected from the functional dependence of α and β. If the measurement times $\Delta\tau_{1,2}$ are chosen to equal a full qubit-resonator swap time (dashed white lines in Fig. 5b,c), the system will be in the state $|Q_1R_aR_bQ_2\rangle = \alpha|e00g\rangle + \beta|g00e\rangle$. An ideal measurement of Q_1 and Q_2 would then yield probabilities $P_{1e} = |\alpha|^2 = \cos^2(\pi g_{1a}\tau)$ and $P_{2e} = |\beta|^2 = \sin^2(\pi g_{1a}\tau)$ for Q_1 and Q_2, respectively, as a function of the transfer time τ. In Figure 5d we display this functional dependence, with a clear 180° phase difference between the two probabilities and the summed probability $P_{1e} + P_{2e}$ close to unity, as expected. The probabilities decrease with τ, owing to the finite energy relaxation of Q_1 and R_a. The decay time of R_b does not contribute noticeably (cf. Supplementary Information). Fitting yields an effective two-resonator decay time approximately equal to the harmonic mean of the relaxation times $T_1^{\text{rel}} \simeq 340\,\text{ns}$ and $T_a^{\text{rel}} \simeq 3.9\,\mu\text{s}$ of Q_1 and R_a, respectively, $T_{ab}^{\text{rel}} \approx (1/2T_1^{\text{rel}} + 1/2T_a^{\text{rel}})^{-1} \simeq 626\,\text{ns}$. We note that the phase qubit enables a photon transfer between R_a and R_b even though the two resonators are separated in frequency by $\simeq 12000$ resonator linewidths.

This last experiment demonstrates a true quantum version of the 'shell game', where the 'pea' (the photon Fock state) is simultaneously hidden under two shells, and the contestant's selection of a shell constitutes a truly probabilistic measurement. More generally, we have experimentally demonstrated an architecture with three resonators and two qubits that displays excellent quantum control over single and double microwave photon Fock states. From a fundamental perspective, these results demonstrate the potential of multi-resonator circuit QED[27,29], both for scientific study and for quantum information.

METHODS

Sample fabrication. The resonators are made from a 150 nm thick rhenium film grown in a molecular-beam-epitaxy system onto a polished sapphire substrate. All the other wiring layers are made from sputtered aluminium with $Al/AlO_x/Al$ Josephson tunnel junctions. All the micro-structures on the different layers are patterned by means of optical lithography and etched by means of inductively coupled plasma etching. Amorphous silicon is used as dielectric insulator for the qubit shunting capacitors and cross-overs. Our sample fabrication clearly shows the flexibility offered by multi-layer processing.

The complete device is then bonded by aluminium wire-bonds to an aluminium sample holder, which is bolted to the mixing chamber of a dilution refrigerator operating at $\simeq 25\,\text{mK}$. A detailed description of the fabrication techniques, electronics and qubit calibration procedures can be found elsewhere[23].

Three-resonator circuit QED Hamiltonian. The Hamiltonian $\widehat{H}$ for the circuit of Fig. 1b can be written as the sum of the Hamiltonians of each unit cell, $\widehat{H}_1$ and $\widehat{H}_2$. Neglecting the driving and dissipative terms for simplicity, the Hamiltonian of the first circuit unit cell can be expressed in the interaction picture with respect to Q_1 and R_a and R_b as the combination of two Jaynes-Cummings interactions:

$$\widehat{H}_1 = h\frac{g_{1a}}{2}\left(\hat{\sigma}_1^+\hat{a}e^{+i2\pi\Delta_{1a}t} + \hat{\sigma}_1^-\hat{a}^\dagger e^{-i2\pi\Delta_{1a}t}\right)$$

$$+ h\frac{g_{1b}}{2}\left(\hat{\sigma}_1^+\hat{b}e^{+i2\pi\Delta_{1b}t} + \hat{\sigma}_1^-\hat{b}^\dagger e^{-i2\pi\Delta_{1b}t}\right), \tag{1}$$

where $\hat{\sigma}_1^{\pm}$ are the rising and lowering operators for Q_1, $\hat{a}, \hat{a}^{\dagger}, \hat{b}$ and $\hat{b}^{\dagger}$ the bosonic annihilation and creation operators for R_a and R_b, respectively, and $\Delta_{1a} \equiv f_1 - f_a$ and $\Delta_{1b} \equiv f_1 - f_b$ the qubit-resonator de-tunings. The Hamiltonian $\hat{H}_2$ for the second circuit unit cell has an analogous expression.

In order to effectively switch off a particular qubit-resonator Q_p-R_q interaction, the condition $\Delta_{pq} \gg g_{pq}$ must be fulfilled. This is the case when Q_1 (Q_2) is at the idle point. On the contrary, when $\Delta_{pq} \to 0$, a resonant Jaynes-Cummings interaction takes place enabling state preparation and transfer in and between the resonators.

References

1. Mabuchi, H. & Doherty, A. C. Cavity Quantum Electrodynamics: Coherence in Context. *Science* **298**, 1372–1377 (2002).

2. Haroche, S. & Raimond, J.-M. *Exploring the Quantum* (Oxford University Press Inc., New York, 2006).

3. Walther, H., Varcoe, B. T. H., Englert, B.-G. & Becker, T. Cavity Quantum Electrodynamics. *Rep. Prog. Phys.* **69**, 1325–1382 (2006).

4. Rauschenbeutel, A., Bertet, P., Osnaghi, S., Nogues, G., Brune, M., Raimond, J.-M. & Haroche, S. Controlled entanglement of two field modes in a cavity quantum electrodynamics experiment. *Phys. Rev. A* **64**, 050301 (2001).

5. Gleyzes, S., Kuhr, S., Guerlin, C., Bernu, J., Deléglise, S., Busk Hoff, U., Brune, M., Raimond, J.-M. & Haroche, S. Quantum Jumps of Light Recording the Birth and Death of a Photon in a Cavity. *Nature (London)* **446**, 297–300 (2007).

6. Deléglise, S., Dotsenko, I., Sayrin, C., Bernu, J., Brune, M., Raimond, J.-M. & Haroche, S. Reconstruction of non-classical cavity field states with snapshots of their decoherence. *Nature (London)* **455**, 510–514 (2008).

7. Hijlkema, M., Weber, B., Specht, H. P., Webster, S. C., Kuhn, A. & A single-photon server with just one atom. *Nature Physics* **3**, 253–255 (2007).

8. Wilk, T., Webster, S. C., Kuhn, A., & Rempe, G. Single-atom single-photon quantum interface. *Science* **317**, 488–490 (2007).

9. Dayan, B., Parkins, A. S., Aoki, T., Ostby, E. P., Vahala, K. J. & Kimble, H. J. A photon turnstile dynamically regulated by one atom. *Science* **319**, 1062–1065 (2008).

10. Papp, S. B., Soo Choi, K., Deng, H., Lougovski, P., van Enk, S. J. & Kimble, H. J. Characterization of multipartite entanglement for one photon shared among four optical modes. *Science* **324**, 764–768 (2009).

11. Wallraff, A., Schuster, D. I., Blais, A., Frunzio, L., Huang, R.-S., Majer, J., Kumar, S., Girvin, S. M. & Schoelkopf, R. J. Strong coupling of a single photon to a superconducting qubit using circuit quantum electrodynamics. *Nature (London)* **431**, 162–167 (2004).

12. Chiorescu, I., Bertet, P., Semba, K., Nakamura, Y., Harmans, C. J. P. M. & Mooij, J. E. Coherent dynamics of a flux qubit coupled to a harmonic oscillator. *Nature (London)* **431**, 159–162 (2004).

13. Johansson, J., Saito, S., Meno, T., Nakano, H., Ueda, M., Semba, K. & Takayanagi, H. Vacuum Rabi oscillations in a macroscopic superconducting qubit LC oscillator system. *Phys. Rev. Lett.* **96**, 127006 (2006).

14. Schoelkopf, R. J. & Girvin, S. M. Wiring up quantum systems. *Nature (London)* **451**, 664–669 (2008).

15. Makhlin, Yu., Schön, G. & Shnirman, A. Quantum-state engineering with Josephson-junction devices. *Rev. Mod. Phys.* **73**, 357–400 (2001).

16. Wendin, G. & Shumeiko, V. S. in *Handbook of Theoretical and Computational Nanotechnology* Vol. 3 (eds. Rieth, M. & Schommers, W.) 223–309 (American Scientific Publishers, Los Angeles, 2006).

17. You, J. Q. & Nori, F. Quantum-state engineering with Josephson-junction devices. *Phys. Today* **58 (11)**, 42–47 (2005).

18. Clarke, J. & Wilhelm, F. K. Superconducting quantum bits. *Nature (London)* **453**, 1031–1042 (2008).

19. Houck, A. A., Schuster, D. I., Gambetta, J. M., Schreier, J. A., Johnson, B. R., Chow, J. M. Frunzio, L., Majer, J. Devoret, M. H., Girvin, S. M. & Schoelkopf, R. J. Generating single microwave photons in a circuit. *Nature (London)* **449**, 328–331 (2007).

20. Sillanpää, M. A., Park, J. I. & Simmonds, R. W. Coherent quantum state storage and transfer between two phase qubits via a resonant cavity. *Nature (London)* **449**, 438–442 (2007).

21. Hofheinz, M., Weig, E. M., Ansmann, M., Bialczak, R. C. Lucero, E., Neeley, M. O'Connell, A. D., Wang, H. Martinis, J. M. & Cleland, A. N. Generation of Fock states in a superconducting quantum circuit. *Nature (London)* **454**, 310–314 (2008).

22. Deppe, F., Mariantoni, M., Menzel, E. P., Marx, A. Saito, S., Kakuyanagi, K. Tanaka, H., Meno, T. Semba, K. Takayanagi, H. Solano, E. & Gross, R. Two-photon probe of the JaynesCummings model and controlled symmetry breaking in circuit QED. *Nature Phsys.* **4**, 686–691 (2008).

23. Hofheinz, M., Wang, H., Ansmann, M., Bialczak, R. C. Lucero, E., Neeley, M. O'Connell, A. D., Sank, D. Sank, D., Wenner, J. Martinis, J. M. & Cleland, A. N. Synthesizing arbitrary quantum states in a superconducting resonator. *Nature (London)* **459**, 546–549 (2009).

24. Wang, H., Hofheinz, M., Ansmann, M., Bialczak, R. C. Lucero, E., Neeley, M., O'Connell, A. D., Sank, D., Weides, M., Wenner, J., Cleland, A. N. & Martinis, J. M. Decoherence dynamics of complex photon states in a superconducting circuit. *Phys. Rev. Lett.* **103**, 3200404 (2009).

25. Leek, P. J., Baur, M., Fink, J. M., Bianchetti, R. Steffen, L., Filipp, S. & Wallraff, A. Cavity QED with separate photon storage and qubit readout modes. *Phys. Rev. Lett.* **104**, 100504 (2010).

26. Johnson, B. R., Reed, M. D., Houck, A. A., Schuster, D. I. Bishop, L. S., Ginossar, E. Gambetta, J. M., DiCarlo, L. Frunzio, L., Girvin, S. M. & Schoelkopf, R. J. Quantum non-demolition detection of single microwave photons in a circuit. *Nature Physics* **DOI: 10.1038/NPHYS1710**, (2010).

27. Mariantoni, M., Deppe, F., Marx, A., Gross, R. Wilhelm, F. K., & Solano, E. Two-resonator circuit quantum electrodynamics: A superconducting quantum switch. *Phys. Rev. B* **78**, 104508 (2008).

28. Sun, C. P., Wei, L. F., Liu, Y. X. & Nori, F. Quantum transducers: integrating transmission lines and nanomechanical resonators via charge qubits. *Phys. Rev. A* **73**, 022318 (2006).

29. Helmer, F., Mariantoni, M., Fowler, A. G., von Delft, J. Solano, E. & Marquardt, F. Cavity grid for scalable quantum computation with superconducting circuits. *Eurphys. Lett.* **85**, 50007 (2009).

30. Walls, D. F. & Milburn, G. J. *Quantum Optics* 2nd ed. (Springer, Berlin-Heidelberg, 2008).

Author Contributions

M.M. performed the experiments with the help of H.W. M.M. analysed the data. M.M. and H.W. fabricated the sample. M.N. provided software infrastructure. J.M.M. and E.L. designed the custom electronics. All authors contributed to the fabrication process, qubit design or experimental set-up, and discussed the data analysis. M.M., J.M.M. and A.N.C. conceived the experiment and co-wrote the paper.

Additional Information

The authors declare no competing financial interests. Supplementary information accompanies this paper.
Correspondence and requests for materials should be addressed to A.N.C.

Supplementary information for 'Photon shell game in three-resonator circuit quantum electrodynamics'

Matteo Mariantoni[1,3,*], H. Wang[1], Radoslaw C. Bialczak[1], M. Lenander[1], Erik Lucero[1], M. Neeley[1], A. D. O'Connell[1], D. Sank[1], M. Weides[1], J. Wenner[1], T. Yamamoto[1,3], Y. Yin[1], J. Zhao[1], John M. Martinis[1,†] and A. N. Cleland[1,‡]

[1] Department of Physics, University of California, Santa Barbara, California 93106, USA

[2] Green Innovation Research Laboratories, NEC Corporation, Tsukuba, Ibaraki 305-8501, Japan

[3] California NanoSystems Institute, University of California, Santa Barbara, California 93106, USA

[*] e-mail: matmar@physics.ucsb.edu

[†] e-mail: martinis@physics.ucsb.edu

[‡] e-mail: anc@physics.ucsb.edu

In this supplementary information, we provide further insight into the transduction fidelity of microwave one- and two-photon Fock states between three coplanar wave guide resonators. In addition, we show that the exponential decay of the two-resonator vacuum Rabi swaps fits very well with a simple harmonic-mean decay model (confirmed by numerical simulations), where both the qubit and resonator energy relaxation times contribute to the effective decay of the two-resonator dynamics.

In order to realize three-resonator circuit quantum electrodynamics (QED) experiments, a complex architecture must be designed and fabricated on a single chip. In the main text (cf. Fig. 1a) we have shown an optical micrograph of the main circuit elements, comprising three coplanar wave guide resonators and two superconducting phase qubits. Figure 1 shows a detail of qubit Q_1, together with its readout SQUID, control and readout lines and the two coupling capacitors to resonators R_a and R_b.

In order to unambiguously verify the high fidelity of transfer of a one-photon Fock state from resonator R_a to resonator R_c via resonator R_b, we have also performed full-state Wigner tomography on R_a and R_c for the two prototypical examples of photon shell game of Fig. 2b(ii),(iv) (cf. main text). The results are displayed in Fig. S. 2, which shows the measured Wigner functions $W(\alpha)$ and corresponding density matrices $\hat{\rho}$ for the Fock state $|1\rangle$ first stored in R_a and then in R_c after transfer via R_b.

The Wigner function is obtained following the steps explained in Ref. 1. In summary, the resonator is first prepared in the desired microwave photon state $|\Psi\rangle$. Second, the resonator is displaced by injecting a coherent state $|-\alpha\rangle$ with complex amplitude $\alpha = |\alpha| \exp(\varphi_\alpha)$, where $|\alpha|$ represents the coherent state real amplitude and φ_α its phase; the state is injected through microwave control lines using a classical pulsed source (cf. Fig. 1a,b). Third, a qubit in its energy ground state is brought into resonance with the resonator for an interaction time long enough to execute several qubit-resonator swaps. Fourth, a simple least-squares fit of these oscillations allows us to obtain the probabilities associated with the different photon number states, from which it is finally possible to obtain the quasi-probability distributions via the parity operator, giving access to full-state Wigner tomography[1–3]. The protocols for calibrating the amplitude and phase of the coherent state used to displace the resonator are explained in detail in Ref. 1. From the Wigner function it is possible to reconstruct the density matrix of the photon state[4,5] $|\Psi\rangle$.
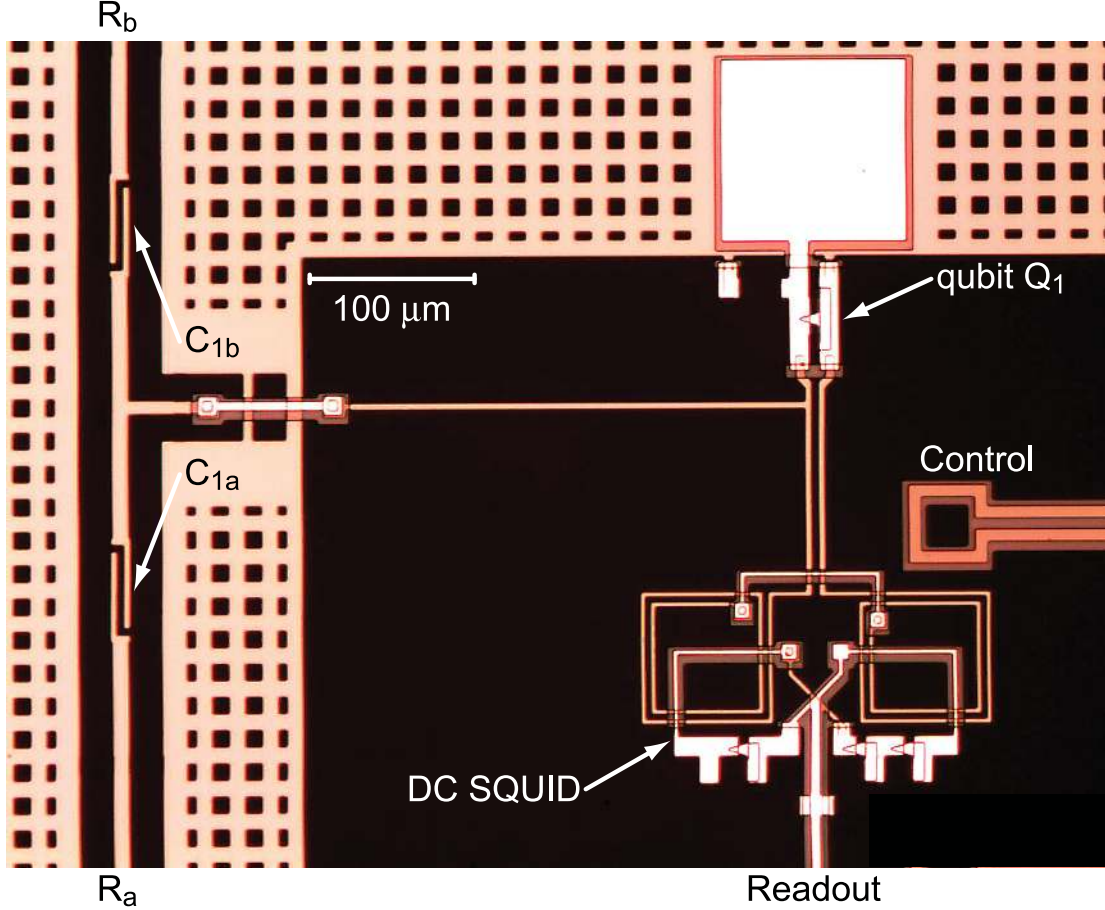
Figure Supplementary 1: **Detail of qubit Q_1 coupled to resonators R_a and R_b.** The capacitors C_{1a} and C_{1b} couple qubit Q_1 (gradiometer design) to resonators R_a and R_b. The qubit state is read out by a DC SQUID (gradiometer design). A portion of the control and readout lines is also visible. A micrometer scale shows the real circuit dimensions.

Given the theoretical and measured density matrices of a photon state $|\Psi\rangle$, $\hat{\rho}_{\text{th}}$ and $\hat{\rho}_{\text{m}}$, respectively, we define the state fidelity as $\mathcal{F} \equiv \text{Tr}\{\hat{\rho}_{\text{th}}\,\hat{\rho}_{\text{m}}\}$. For the Fock state $|1\rangle$ prepared in R_a, with the associated Wigner function and density matrix of Fig. S. 2a,c, we find $\mathcal{F} \simeq 0.84$. This compares well with the amplitude of the fit to the qubit-resonator swaps, which gives a fidelity $\mathcal{F} \simeq 0.86$ (cf. Fig. 2 in main text). After being transferred to R_c, the state has the Wigner function and density matrix of Fig. 2b,d and the corresponding fidelity $\mathcal{F} \simeq 0.64$, which is also consistent with the fidelity found with the simple least-squares fit (cf. Fig. 2 in main text). The loss of fidelity occurring during the photon transfer between the three resonators can be attributed to qubit decoherence and slight calibration errors during the swap qubit-resonator operations. Nevertheless, it is remarkable that the density matrix associated with the state in R_c is still very pure, with nearly negligible spurious matrix elements and only a small contribution from the $|0\rangle$ state.

Other two relevant figures of merit for the transfer of one- and two-photon Fock states between resonators R_a, R_b and R_c are represented by the harmonic purity of the state (i.e. absence of beatings) and the $\sqrt{2}$ scaling factor between swaps associated with the Fock states[6] $|1\rangle$ and $|2\rangle$. These properties can easily be estimated by computing the fast Fourier transform (FFT) of the qubit-resonator vacuum Rabi swaps. Figure Supplementary 3 shows the FFTs of the Rabi swaps for the key steps of the photon shell game and 'Towers of Hanoi', i.e. for a Fock $|1\rangle$ and $|2\rangle$ created in R_a and measured with Q_1, then transferred to R_b and measured with Q_1 and Q_2, and finally transferred to R_c and measured with Q_2. The time-domain swaps used to compute the FFTs are those in Figs. 2b and 3 in main text.
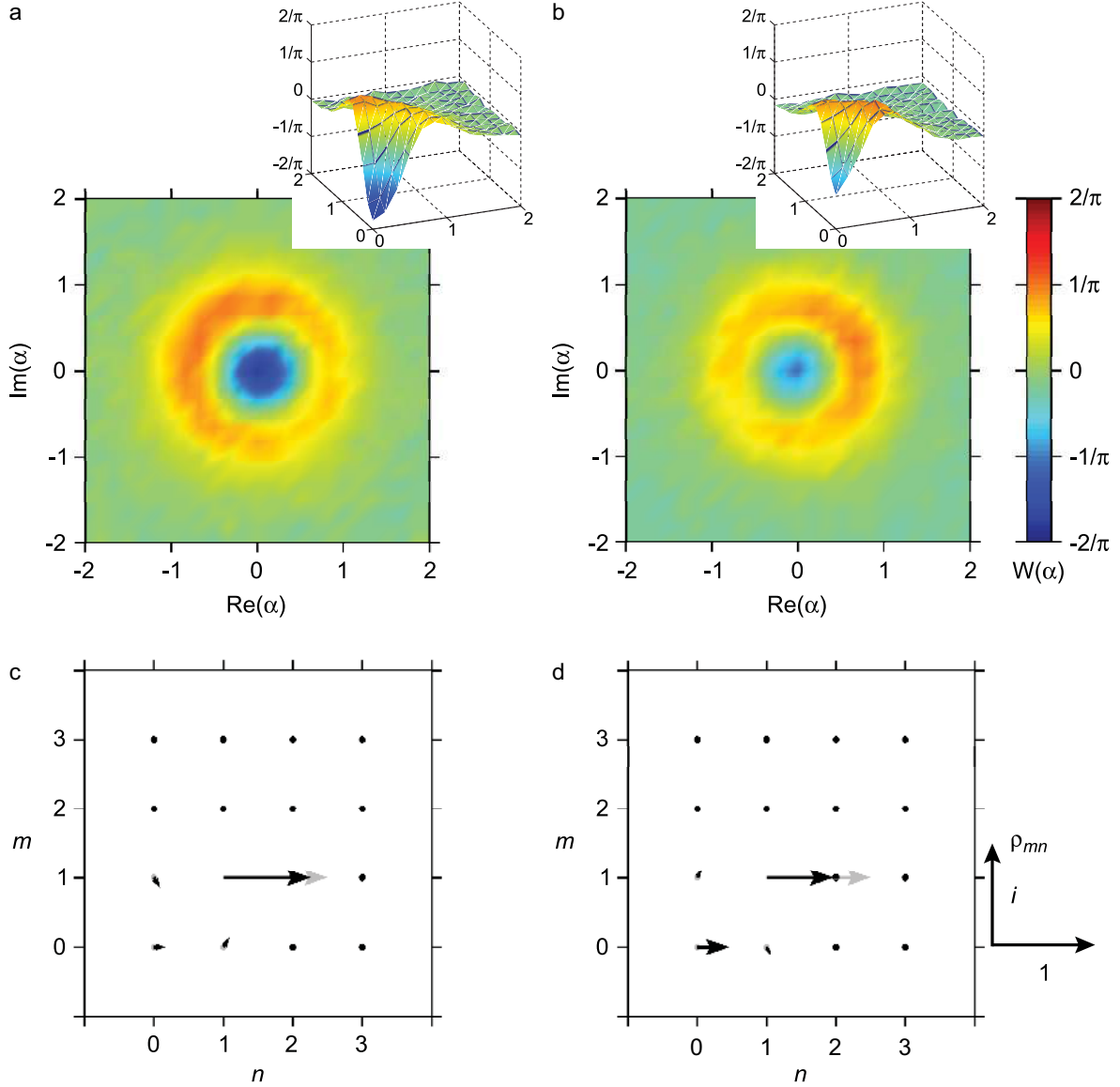
Figure Supplementary 2: **Wigner tomography for the photon shell game. a,** Measured Wigner function $W(\alpha)$ for resonator R_a as a function of the complex resonator amplitude α in square root of photon number units (colour scale bar on the far right). The inset displays a cut of the three-dimensional plot of the Wigner function. **b,** Same as in **a**, but for resonator R_c (colour scale bar on the right). Negative quasi-probabilities clearly indicate the quantum-mechanical nature of the intra-resonator states. **c,** Theoretical (grey) and measured (black) values for the density matrix associated with the state stored in resonator R_a, $\hat{\rho}$, projected onto the number states $\rho_{mn} \equiv \langle m|\hat{\rho}|n\rangle$. The magnitude and phase of ρ_{mn} is represented by the length and direction of an arrow in the complex plane (the scale for the real and imaginary part is reported on the far right). **d,** Same as in **c**, but for resonator R_c. When representing the density matrices, the resonator Hilbert space has been truncated to the lowest four bosonic states.

    The last topic to be considered in this supplementary is the energy relaxation mechanism of the two-resonator Rabi swaps of Fig. 5d in the main text.

    In order to gain deeper insight into the decay dynamics of the two-resonator Rabi, we first need information on the energy relaxation times of qubit Q_1 and resonators R_a and R_b. Figure Supplementary 4 shows the experimental measurement of these decay times. Note that the resonators' energy relaxation time is determined by preparing the resonator in a one-photon Fock state $|1\rangle$, and storing it for a variable time. After this time, a qubit is brought on resonance with the resonator, the state swapped into the qubit, and the qubit population then read out[7,8].

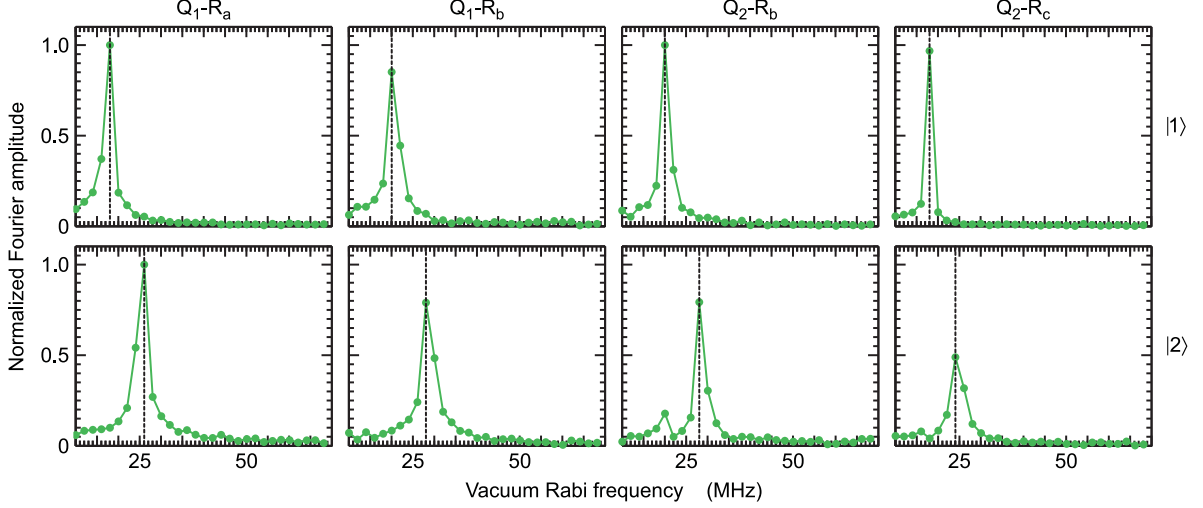   The energy relaxation times obtained from a simple exponential fit are reported in Table S. 1. We

Figure Supplementary 3: **Fourier analysis for the photon shell game and 'Towers of Hanoi'.** Top sub-panels, normalized Fourier amplitude as a function of vacuum Rabi frequency associated with the qubit-resonator Rabi swaps for a one-photon Fock state $|1\rangle$. Bottom sub-panels, normalized Fourier amplitude for a two-photon Fock state $|2\rangle$. Above each column is indicated the respective qubit-resonator interaction. The dashed black line in each sub-panel indicates the maximum Fourier component. The amplitude re-normalization is calculated with respect to the largest Fourier component for Fock state $|1\rangle$ (top sub-panels) and $|2\rangle$ (bottom sub-panels), respectively. The $\sqrt{2}$ scaling [1] between the $|1\rangle$ and $|2\rangle$ states is clearly visible. The absence of beatings (only a small beating, owing to some residual presence of state $|1\rangle$, for state $|2\rangle$ in the Q_2-R_b sub-panel) shows the high level of harmonic purity of the states transferred between the three resonators, both for the photon shell game and for the more complex 'Towers of Hanoi'.

use the qubit and resonator energy relaxation times as well as the other parameters listed in the table to solve numerically a Lindblad-type master equation [9,10]:

$$\dot{\hat{\rho}} = \frac{1}{i\hbar}(\widehat{H}_1 \hat{\rho} - \hat{\rho}\widehat{H}_1) + \sum_{k=1}^{3} \hat{\mathcal{L}}_k \hat{\rho}, \qquad (2)$$

where $\dot{\hat{\rho}} \equiv (\partial/\partial t)\,\hat{\rho}$ is the time derivative of the total density matrix $\hat{\rho}$ describing the system, $\widehat{H}_1$ is the Hamiltonian of Eq. (1) (cf. Methods' section in main text), $\hat{\mathcal{L}}_k$ is the Lindblad superoperator defined as $\hat{\mathcal{L}}_k \hat{\rho} \equiv \gamma_k(\hat{X}_k\hat{\rho}\hat{X}_k^\dagger - \hat{X}_k^\dagger\hat{X}_k\hat{\rho}/2 - \hat{\rho}\hat{X}_k^\dagger\hat{X}_k/2)$ and $k \in \mathbb{N}$. The qubit and resonators decay rates are defined as $\gamma_1 \equiv 1/T_a^{rel}$, $\gamma_2 \equiv 1/T_1^{rel}$ and $\gamma_3 \equiv 1/T_b^{rel}$ and the generating operators as $\hat{X}_1 \equiv \hat{a}$, $\hat{X}_1^\dagger \equiv \hat{a}^\dagger$, $\hat{X}_2 \equiv \hat{\sigma}^-$, $\hat{X}_2^\dagger \equiv \hat{\sigma}^+$, $\hat{X}_3 \equiv \hat{b}$ and $\hat{X}_3^\dagger \equiv \hat{b}^\dagger$. We numerically solve Eq. (2) for the pulse sequence shown in Fig. 5a (cf. main text), without accounting for the measurement process. The results are displayed in Fig. S. 5, where they are compared to the experimental data.

Figure Supplementary 5a,c shows the same data as in Fig. 5d, but for a transfer time τ three times longer. Furthermore, the data shown in Fig. S. 5a,c were taken using a different device compared to Fig. 5d, with longer qubit relaxation times. The exponential decay obtained by the simple harmonic mean model (cf. main text) is superposed with the data, making evident the qualitative validity of the model. Figure Supplementary 5b,d shows the results of the simulations of Eq. (2) corresponding to the experimental data of Fig. S. 5a,c, respectively. Data and simulations are in very good agreement, supporting the simple harmonic mean decay model. In particular, the experimental decay time obtained by fitting the data is $\simeq 840\,\mathrm{ns}$, from simulations $\simeq 874\,\mathrm{ns}$ and from the harmonic mean model $\simeq 896\,\mathrm{ns}$. The amplitude of the simulated two-resonator Rabi swaps was adjusted to the measured amplitudes. The slight discrepancy between the experimental data and simulations for the low region of the occupation probabilities (causing an offset between data and simulations) is because the simulations do not account for the measurement process. Notice that we can safely assume that only qubit Q_1 and resonator R_a, swapping for a variable transfer time τ, contribute to the effective decay mechanism of the two-resonator
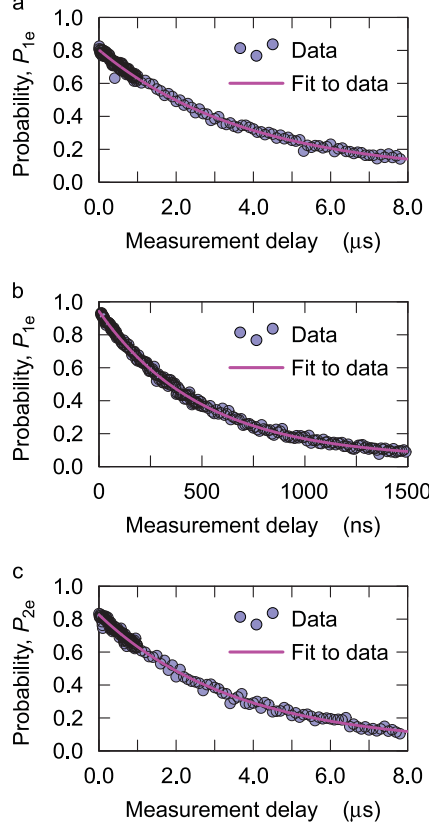
14

Figure Supplementary 4: **Energy relaxation for qubit Q$_1$ and resonators R$_\mathbf{a}$ and R$_\mathbf{b}$**. In all panels: $P_{p\mathrm{e}}$ is the probability to find Q$_p$ in $|e\rangle$ as a function of measurement delay time (i.e. the time a photon is stored in the resonator before being swapped into the qubit). Full circles are data and solid magenta lines exponential fits to data. **a,** Measurement of the energy relaxation of resonator R$_\mathrm{a}$ using qubit Q$_1$ as a detector[7,8]. **b,** Energy relaxation of qubit Q$_1$. **c,** Same as in **a**, but for resonator R$_\mathrm{b}$.

Rabi dynamics. In fact, the second resonator serves only as a mapping resonator, the state of which is measured with Q$_2$ typically after a time $\Delta\tau_2 \ll T_\mathrm{b}^\mathrm{rel}$ (cf. main text and Fig. 5b,c). In other words, examining the two-dimensional plots of Fig. 5b,c we expect two distinct decay mechanisms. The first along the horizontal axis ($\Delta\tau_1$ and $\Delta\tau_2$). This decay is practically negligible as this measurement is completed in $\leqslant 30\,\mathrm{ns}$. The second is along the vertical axis (τ) related to the Q$_1$-R$_\mathrm{a}$ swaps, as explained above.

For a theoretical analysis of the decay mechanisms characteristic of two-resonator dynamics in different regimes we remind to Ref. 13.

Table Supplementary 1: **Main parameters used for the numerical simulations of the two-resonator Rabi dynamics.** δ represents the non-linearity of the superconducting phase qubit, i.e. the energy difference in unit Hz between the qubit transition frequencies relative to the ground state and first excited state and to the first excited state and second excited state, respectively[12]. The non-linearity has been used in the simulations to take into account possible leakage outside of the qubit subspace. T_a^ϕ and T_b^ϕ are the dephasing times for resonators R_a and R_b, respectively. Since our main goal is to understand the energy relaxation of the two-resonator Rabi swaps, the qubit dephasing time T_1^ϕ has been neglected in the simulations. All the other parameters are defined in the main text.

$\mathbf{R_a}$	f_a (GHz)	–	g_{1a} (MHz)	T_a^{rel} (ns)	T_a^ϕ (ns)
	6.340		17.95	3881	$\gg T_a^{\text{rel}}$
$\mathbf{Q_1}$	f_1 (GHz)	δ (MHz)	–	T_1^{rel} (ns)	T_a^ϕ (ns)
	6.563	204.23		507	– –
$\mathbf{R_b}$	f_b (GHz)	–	g_{1b} (MHz)	T_b^{rel} (ns)	T_b^ϕ (ns)
	6.815		20.25	3549	$\gg T_b^{\text{rel}}$

As a last remark, it is worth mentioning that all data shown in the main text and supplementary information were corrected for measurement errors, following the standard procedure outlined in Ref. 11.

In conclusion, in this supplementary information we have validated the experimental results and conclusions presented in the main text by means of full-state Wigner tomography, FFT analysis and numerical simulations.
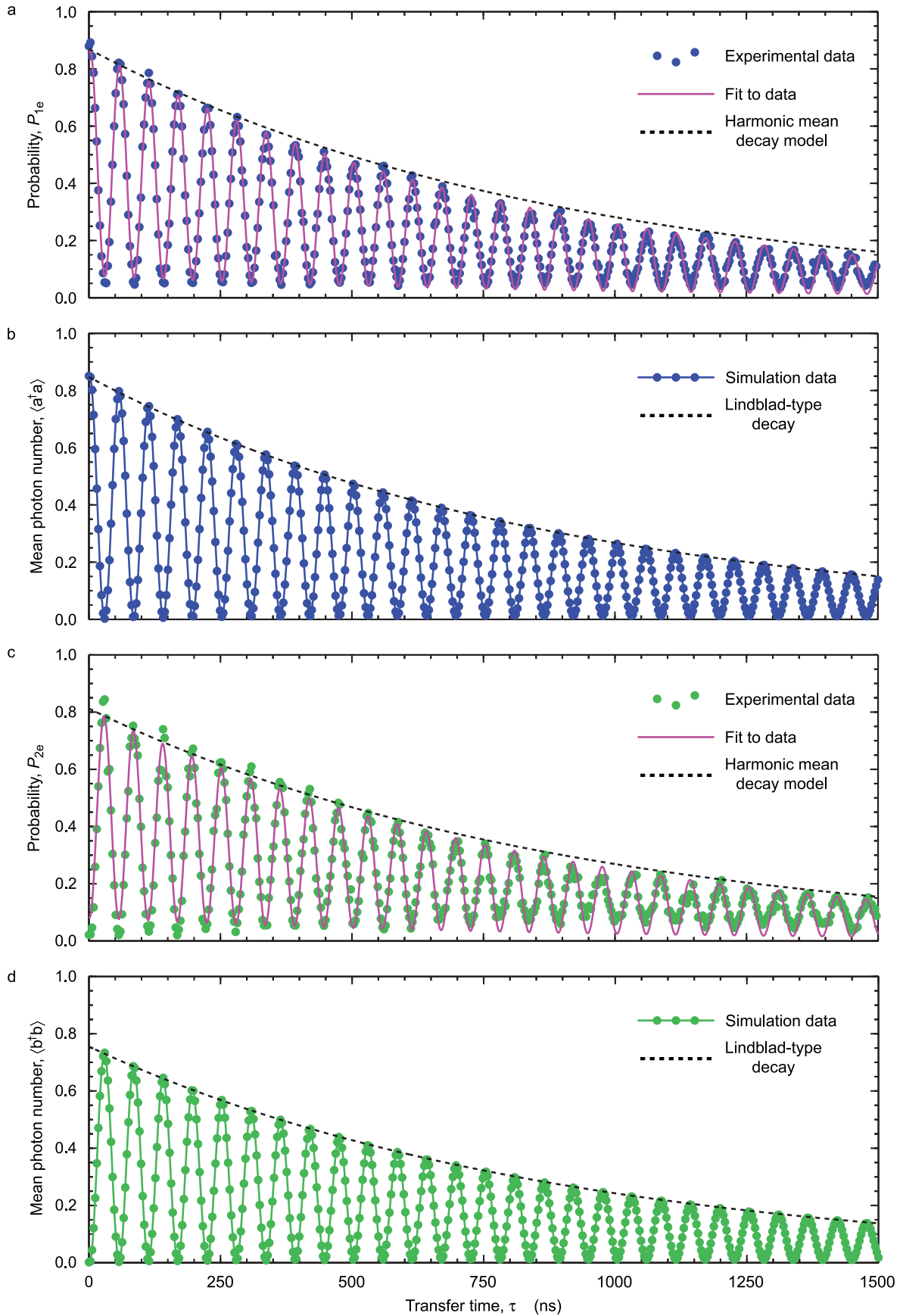
Figure Supplementary 5: **Comparison between experimental results and numerical simulations of two-resonator Rabi swaps. a,** R_a state dynamics measured as the probability P_{1e} to find Q_1 in the excited state versus transfer time τ. Dark blue circles are data, solid magenta line a least-squares fit to data and dashed black line the exponential harmonic mean decay. **b,** Simulation (parameters in Table S. 1) of the data in **a**, showing the resonator mean photon number $\langle \hat{a}^\dagger \hat{a} \rangle$ versus τ. The exponential decay envelope (dashed black line) confirms the harmonic mean decay model. **c,** Same as in **a**, but for R_b (cf. main text). Light green circles are data, solid magenta line a least-squares fit to data and dashed black line the exponential harmonic mean decay. **d,** Same as in **b**, but for R_b.

References

1. Hofheinz, M., Wang, H., Ansmann, M., Bialczak, R. C. Lucero, E., Neeley, M. O'Connell, A. D., Sank, D. Sank, D., Wenner, J. Martinis, J. M. & Cleland, A. N. Synthesizing arbitrary quantum states in a superconducting resonator. *Nature (London)* **459**, 546–549 (2009).

2. Haroche, S. & Raimond, J.-M. *Exploring the Quantum* (Oxford University Press Inc., New York, 2006).

3. Leonhardt, U. *Measuring the Quantum State of Light* (Cambridge University Press, Cambridge, 1997).

4. Leibfried, D., Meekhof, D. M., King, B. E., Monroe, C., Itano, W. M. & Wineland, D. J. Experimental determination of the motional quantum state of a trapped atom. *Phys. Rev. Lett.* **77**, 4281-4285 (1996).

5. Bertet, P., Auffeves, A., Maioli, P., Osnaghi, S., Meunier, T., Brune, M., Raimond, J.-M. & Haroche, S. Direct measurement of the Wigner function of a one-photon Fock state in a cavity. *Phys. Rev. Lett.* **89**, 200402 (2002).

6. Hofheinz, M., Weig, E. M., Ansmann, M., Bialczak, R. C. Lucero, E., Neeley, M. O'Connell, A. D., Wang, H. Martinis, J. M. & Cleland, A. N. Generation of Fock states in a superconducting quantum circuit. *Nature (London)* **454**, 310–314 (2008).

7. Neeley, M., Ansmann, M., Bialczak, R. C. Hofheinz, M. Katz, N. Lucero, E., O'Connell, A., Wang, H., Cleland, A. N. & Martinis, J. M. Process tomography of quantum memory in a Josephson-phase qubit coupled to a two-level state. *Nature Physics* **4**, 523–526 (2008).

8. Wang, H., Hofheinz, M., Ansmann, M., Bialczak, R. C. Lucero, E., Neeley, M. O'Connell, A. D., Sank, D. Wenner, J., Cleland, A. N. & Martinis, J. M. Measurement of the decay of Fock states in a superconducting quantum circuit. *Phys. Rev. Lett.* **101**, 240401 (2008).

9. Walls, D. F. & Milburn, G. J. *Quantum Optics* 2nd ed. (Springer, Berlin-Heidelberg, 2008).

10. Blais, A., Huang, R.-S., Wallraff, A., Girvin, S. M. & Schoelkopf, R. J. Cavity quantum electrodynamics for superconducting electrical circuits: An architecture for quantum computation. *Phys. Rev. A* **69**, 062320 (2004).

11. Ansmann, M., Wang, H., Bialczak, R. C., Hofheinz, M., Lucero, E., Neeley, M., O'Connell, A. D., Sank, D., Weides, M., Wenner, J., Cleland, A. N. & Martinis, J. M. Violation of Bell's inequality in Josephson phase qubits. *Nature (London)* **461**, 504–506 (2009).

12. Lucero, E., Kelly, J., Bialczak, R. C., Lenander, M., Mariantoni, M., Neeley, M., O'Connell, A. D., Sank, D., Wang, H., Weides, M., Wenner, J., Yamamoto, T., Cleland, A. N. & Martinis, J. M. Reduced phase error through optimized control of a superconducting qubit. *eprint arXiv* **1007.1690**, (2010).

13. Reuther, G. M., Zueco, D., Deppe, F., Hoffmann, E., Menzel, E. P., Weißl, T., Mariantoni, M., Kohler, S., Marx, A., Solano, E., Gross, R., & Hänggi, P. Two-resonator circuit quantum electrodynamics: dissipative theory. *Phys. Rev. B* **81**, 144510 (2010).